7944 *Macromolecules* **1998,** *31,* 7944−7952

Molecular Dynamics of Atactic Polypropylene Melts

Stelios J. Antoniadis, Christina T. Samara, and Doros N. Theodorou*

Molecular Modelling of Materials Laboratory, Institute of Physical Chemistry, National Research Centre for Physical Sciences "Demokritos", GR 15310 Ag. Paraskevi Attikis, Greece, and Department of Chemical Engineering, University of Patras, GR 26500 Patras, Greece

Received May 7, 1998; Revised Manuscript Received August 6, 1998

ABSTRACT: A molecular model suitable for predicting thermodynamic and dynamical properties of polypropylene is developed. A systematic effort is undertaken to improve the representation of the potential. Molecular dynamics (MD) simulations of atactic polypropylene, based on the new potential, indicate good agreement of volumetric properties and of the solubility parameter with experimental data for a wide range of temperatures and pressures. To characterize the system dynamics at the segmental level, time autocorrelation functions have been computed for pendant ($C-CH_3$) bonds and skeletal torsion angles. Predicted correlation times are in good agreement with NMR measurements. An analysis of conformational transitions reveals the development of spatial heterogeneity in the segmental mobility at constant observation time; this heterogeneity increases strongly with decreasing temperature. The rate of conformational isomerizations in the polymer has been analyzed by constructing a hazard plot of first passage times, which indicates a sharp decrease in the number of bonds capable of conformational transition at low temperature.

1. Introduction

The ability to predict the properties of polymeric materials from the chemical constitution of chains is critical in the selection, improvement, and design of polymer products in an industrial setting. Molecular simulation techniques provide a means of predicting macroscopic properties, as well as elucidating the molecular mechanisms that underlie structure/property relationships. Particularly important from the point of view of applications are vinyl polymers, as they offer the opportunity to tailor properties through appropriate selection of the tacticity of chains. In this work we focus on a representative vinyl polymer, polypropylene (PP). There has been considerable modeling work on polypropylene.[1−6] Both explicit-atom and united-atom representations have been used for the skeletal segments, with methyl groups treated as single united atoms. Several simulation techniques have been employed, such as molecular mechanics,[1] molecular dynamics,[2−4] and Monte Carlo[5] for the purpose of predicting elastic constants in the glassy state, melt, and glass *PVT* properties, surface tension, gas solubility, and some aspects of dynamical behavior. Despite the encouraging results obtained, the polypropylene models used in these past investigations have not been completely satisfactory. In this work, we develop a molecular model suitable for predicting *thermodynamic and dynamical* properties of polypropylene melts of various tacticities over a wide range of temperatures and pressures. The model and the simulation algorithms that we construct must not only reflect the behavior of the real systems but also afford high numerical efficiency. Systematic effort has been undertaken to improve the representation of the potential so as to capture thermodynamic properties in well-equilibrated systems.

The molecular model and simulation method are presented in section 2 of this paper. Results on thermodynamics, structure, and segmental dynamics are presented and discussed in section 3, followed by a statement of conclusions drawn from this work (section 4). Finally, some mathematical details are given in the Appendix.

2. Molecular Model and Simulation Method

The model system consisted of $N_{\mathrm{ch}} = 2$ molecules of degree of polymerization $N_{\mathrm{un}} = 76$ in a cubic cell of initial side 23.42 Å, with periodic boundary conditions. In our model, the chains consist of carbon (C), hydrogen (H), and methyl (R) Lennard-Jones (LJ) interaction sites. Skeletal sites are numbered 0, 1, 2, ..., $2N_{\mathrm{un}}$, sites 0 and $2N_{\mathrm{un}}$ being methyl groups. Odd-numbered skeletal carbons are chiral, bearing one pendant hydrogen, while even-numbered carbons are achiral. C−C and C−R bond lengths are fixed at 1.54 Å, while CCC and CCR skeletal bond angles are flexible. All mass is assumed to be concentrated on R and C sites; i.e., the mass of each hydrogen is collapsed onto the carbon atom to which it is connected. Positions of pendant hydrogens are uniquely determined by the surrounding heavy (C and R) interaction sites, with C−H bonds kept constant at $l_{\mathrm{H}} = 1.10$ Å, as follows. For a hydrogen H_i connected to chiral skeletal carbon C_i the requirement is that $\mathrm{C}_i\mathrm{H}_i$ remain perpendicular to the plane $\mathrm{C}_{i-1}\mathrm{C}_{i+1}\mathrm{R}_i$ at all times (see Figure 1a). Considering the backbone in all-trans conformation, we assign an index $c = +1$ to all pendant atoms on one side of the skeletal plane and $c = -1$ to all pendant atoms on the other side, according to the following convention: c is +1 for a hydrogen H_i connected to a chiral carbon C_i that is nearer the chain start than the chain end if that carbon is in an *S* configuration. The exact position of H_i is then

$$\mathbf{r}_{\mathrm{H}_i} = \mathbf{r}_{\mathrm{C}_i} + c l_{\mathrm{H}} \frac{(\mathbf{r}_{\mathrm{R}_i} - \mathbf{r}_{\mathrm{C}_i-1}) \times (\mathbf{r}_{\mathrm{R}_i} - \mathbf{r}_{\mathrm{C}_i+1})}{|(\mathbf{r}_{\mathrm{R}_i} - \mathbf{r}_{\mathrm{C}_i-1}) \times (\mathbf{r}_{\mathrm{R}_i} - \mathbf{r}_{\mathrm{C}_i+1})|} \quad (1)$$

---

* Author to whom correspondence should be addressed at the University of Patras. Phone: +3061-997-398. Fax: +3061-993-255. E-mail: doros@sequoia.chemeng.upatras.gr.

10.1021/ma9807318 CCC: $15.00

Table 1. Simulation Parameters

	HH	CH	RH	CC	CR	RR
			Local			
σ_{ij} (Å)	2.3160	2.7615	2.9400	3.2070	3.3855	3.5640
ϵ_{ij} (kcal/mol)	0.0763	0.0801	0.1029	0.0841	0.1080	0.1388
			Nonlocal			
σ_{ij} (Å)	2.5010	2.9825	3.1320	3.4640	3.6135	3.7630
ϵ_{ij} (kcal/mol)	0.0526	0.0554	0.0765	0.0584	0.0806	0.1113

bond angles	R−C−C	C−C−R	aC−C−C	cC−C−C	R−C−R
θ^0_{ijk} (rad)	1.9465	1.9465	1.8778	1.9380	2.0560

c^{θ}_{ijk} (kcal mol^{-1} rad^{-2})	115
c^{ϕ}_{ijkl} (kcal mol^{-1})	2.8
W (g mol^{-1} Å^{-4})	10
Q (kcal ps^2 mol^{-1})	0.0517

where c equals $+1$ for S-chirality and -1 for R-chirality of C_i. For the geminal hydrogens H_i^+ and H_i^- connected to an achiral carbon C_i, we require that the plane $H_i^+C_iH_i^-$ be perpendicular to plane $C_{i-1}C_iC_{i+1}$, that angles $H_i^+C_iH_i^-$ and $C_{i-1}C_iC_{i+1}$ have a common bisector, and that angle $H_i^+C_iH_i^-$ be fixed at $\pi - \theta_H$, where $\theta_H = 1.28$ rad (see Figure 1b). Setting

$$\hat{\mathbf{b}}_i = \frac{\mathbf{r}_{C_i} - \mathbf{r}_{C_i-1}}{|\mathbf{r}_{C_i} - \mathbf{r}_{C_i-1}|} \tag{2}$$

and

$$\hat{\mathbf{u}}_i = \frac{\hat{\mathbf{b}}_i - \hat{\mathbf{b}}_{i+1}}{\sqrt{2(1 - \hat{\mathbf{b}}_i\cdot\hat{\mathbf{b}}_{i+1})}} \qquad \hat{\mathbf{v}}_i = \frac{\hat{\mathbf{b}}_i \times \hat{\mathbf{b}}_{i+1}}{|\hat{\mathbf{b}}_i \times \hat{\mathbf{b}}_{i+1}|} \tag{3}$$

where $\hat{\mathbf{u}}_i$ is the unit vector along the bisector of angle $C_{i-1}C_iC_{i+1}$ in the direction from C_i toward H_i^+ and H_i^-, and $\hat{\mathbf{v}}_i$ is a unit vector normal to plane $C_{i-1}C_iC_{i+1}$. The positions of the hydrogens are given by

$$\mathbf{r}_{H_i^{\pm}} = \mathbf{r}_{C_i} + l_H\left(\sin\frac{\theta_H}{2}\mathbf{u}_i \pm \cos\frac{\theta_H}{2}\mathbf{v}_i\right) \tag{4}$$

Making the hydrogens centers of force with positions determined uniquely by the surrounding "heavy atoms" C and R, but not centers of mass, simplifies the form of the dynamical equations and allows using longer time steps in the integration algorithm when doing MD simulations, since high-frequency motions of hydrogens are excluded.

Along a chain, all pairs of sites separated by more than two bonds interact through LJ potentials

$$V^{LJ}_{ij}(r_{ij}) = 4\epsilon_{ij}\left\{\left(\frac{\sigma_{ij}}{r_{ij}}\right)^{12} - \left(\frac{\sigma_{ij}}{r_{ij}}\right)^{6}\right\} \tag{5}$$

with r_{ij} being the scalar minimum image distance between sites i and j. Potential tails are cut at $1.45\sigma_{ij}$ and brought smoothly to zero at $2.33\sigma_{ij}$ using a quintic spline.[1] Local intramolecular interactions (between interaction sites up to four bonds apart) are described by the same set of σ and ϵ parameters as in ref 1, while a different set is used for nonlocal and intermolecular interactions.[12−14] This choice was motivated by the observation that the parameters of ref 1 give satisfactory conformational statistics but too high melt densities. The modified (σ, ϵ) values for nonlocal interactions were arrived at by a strategy similar to that used in ref 14 for polyethylene. The sets of (σ, ϵ) parameters used for local and nonlocal interactions are listed in Table 1. Long-range attractions between atomic pairs are accounted for by direct integration of the LJ potentials, assuming radial distribution functions of 1 at separations greater than $1.45\sigma_{ij}$.

A simple harmonic potential is used to keep the bond angle formed between three heavy interaction sites i, j, k (C or R) near its equilibrium value θ^0_{ijk}

$$V^{\theta}_{ijk} = c^{\theta}_{ijk}(\theta_{ijk} - \theta^0_{ijk})^2 \tag{6}$$

A 3-fold symmetric torsional potential is used for all nonterminal dihedral angles

$$V^{\phi}_{ijkl} = \frac{1}{2}c^{\phi}_{ijkl}[1 - \cos(3\phi_{ijkl})] \tag{7}$$

where i, j, k, l are skeletal carbons. Parameters for bond angle and torsion angle potentials were taken from Sylvester *et al.*[2] and are listed in Table 1. A stiff 4-body potential is introduced to prevent flips in the chirality of the skeletal carbons[6]

$$V^{\text{chir}}(f_{\text{chir}}) = \frac{\kappa}{1 - f_{\text{chir}}} - \frac{\kappa}{(1-\delta)^3}f_{\text{chir}}^{\ 2} + \frac{\kappa}{(1-\delta)^2}(3\delta - 1)f_{\text{chir}} - \frac{\kappa}{(1-\delta)^3}(3\delta^2 - 3\delta + 1) \tag{8}$$

where

$$f_{\text{chir}} = \frac{\cos^2\alpha + \cos^2\beta + 2\cos\alpha\cos\beta\cos\theta}{\sin^2\theta} \le 1$$

with $\pi - \alpha$, $\pi - \beta$, and $\pi - \theta$ denoting the CCR, RCC, and CCC bond angles around a chiral carbon (see Figure 1a). The values of δ and κ are 0.4 and 0.05, respectively, and are selected to give a smooth potential in order to avoid dramatic decreases in time step in the course of the integration of the equations of motion.

Our potential parametrization was first tested on liquid 2,4-dimethylpentane over temperatures ranging from 300 to 373 K and pressures ranging from 10 to 100 MPa. This low molecular weight liquid can safely be equilibrated completely by molecular dynamics or Monte Carlo with modest computational resources. Predictions for PVT behavior and self-diffusivities were found to be in very good agreement with available experimental evidence.

To study the behavior of the above model for polypropylene, we first use the MD approach. Our simulations

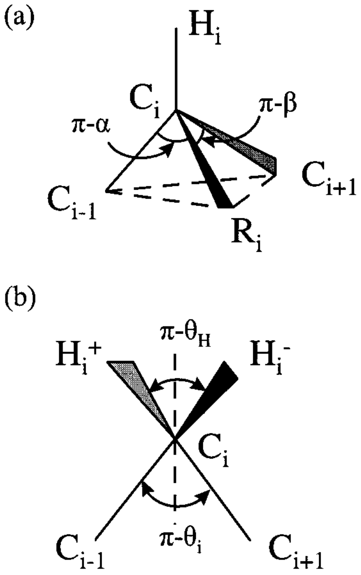

Figure 1. Representation of local geometry at (a) a chiral carbon and (b) at an achiral carbon.

are carried out in the isothermal–isobaric (*NPT*) ensemble using the extended ensemble technique of Nosé and Klein.[7] Forces are calculated for all interaction sites and transferred to heavy atoms only (C and R) through geometric derivatives, as shown in eq 11 below. Newton's equations of motion for heavy atoms are integrated in Cartesian coordinates with a Gear fifth-order predictor–corrector scheme.[8] Forces resulting from the bond length constraints are computed by the algorithm of Edberg, Evans, and Morriss.[9] A Fixman potential[10] is introduced to compensate for the C–C and C–R bond length constraints (see Appendix A). As a result, the dynamically simulated model behaves as a flexible model in the limit of infinite stiffness and is fully consistent with the configuration-space probability density sampled in our Monte Carlo simulations of PP.

To summarize, the total potential energy is computed as

$$V_{\text{tot}} = V^{\text{LJ}} + V^{\theta} + V^{\phi} + V^{\text{chir}} + V^{\text{F}} \tag{9}$$

V^{LJ} is computed as a sum of inter- and intramolecular nonbonded interactions, while V^{θ}, V^{ϕ}, and V^{chir} are sums calculated along the contours of all chains present in the system. V^{F} is a sum of terms computed recursively for each chain as outlined in Appendix A. The Lagrangian has the form

$$L = \sum_i \frac{m_i}{2} s^2 \dot{\mathbf{r}}_i^{\,2} - V_{\text{tot}} + \frac{Q}{2}\dot{s}^2 - f k_{\text{B}} T \ln s + \frac{9}{2} W L^4 \dot{L}^2 - P_{\text{ex}} L^3 \tag{10}$$

where $f = (6N_{\text{un}} + 3)N_{\text{ch}}$ is the number of degrees of freedom of the system, s is the "bath" degree of freedom used to control the temperature, L is the box edge length, W and Q are the inertial parameters associated with s and L, respectively, and P_{ex} is the externally set pressure. The sum over i extends over all heavy atoms in the system. The equations of motion are derived from the Lagrangian, eq 10, with consideration of the holonomic constraints of constant bond lengths through the procedure described in ref 15, p 47, eq 2–29.

$$m_i s^2 \ddot{r}_i^{\zeta} + 2 m_i s \dot{s} \dot{r}_i^{\zeta} + \frac{\partial V^{\theta}}{\partial r_i^{\zeta}} + \frac{\partial V^{\phi}}{\partial r_i^{\zeta}} + \sum_j \frac{\partial V_{ij}^{\text{LJ}}}{\partial r_{ij}} \frac{(r_i^{\zeta} - r_j^{\zeta})}{r_{ij}} - \sum_k \frac{1}{r_{ik}} \frac{\partial V_{ik}^{\text{LJ}}}{\partial r_{ik}} \sum_{\eta} (r_i^{\eta} - r_k^{\eta}) \frac{\partial r_k^{\eta}}{\partial r_i^{\zeta}} + \sum_p \sum_q \frac{1}{r_{pq}} \frac{\partial V_{pq}^{\text{LJ}}}{\partial r_{pq}} \sum_{\eta} \frac{(r_p^{\eta} - r_q^{\eta})}{r_{pq}} \frac{\partial r_p^{\eta}}{\partial r_i^{\zeta}} + \frac{\partial V^{\text{chir}}}{\partial r_i^{\zeta}} + \frac{\partial V^{\text{F}}}{\partial r_i^{\zeta}} = s^2 \sum_l \lambda_n (r_i^{\zeta} - r_l^{\zeta}) \tag{11}$$

$$\ddot{L} = \frac{s^2}{2L^2 W}(P_{\text{int}} - P_{\text{ex}}) + \frac{\dot{s}}{s}\dot{L} - 2\frac{\dot{L}^2}{L} \tag{12}$$

$$\ddot{s} = \frac{s}{Q}\Big[\sum_i m_i \dot{\mathbf{r}}_i^{\,2} - f k_{\text{B}} T\Big] + \frac{\dot{s}^2}{s} \tag{13}$$

where the indices j, k, p, q, l have the following meanings: j, heavy atom interacting with i; k, hydrogen interacting with i, whose position depends on i; p, hydrogen whose position depends on i; q, any center (heavy atom or hydrogen) interacting with p; l, heavy atom bonded to atom i; n, index of the bond connecting heavy atoms i and l. Superscripts ζ and η denote the components of position vectors and of their time derivatives (ζ, $\eta = x, y, z$). The coefficients λ_n are Lagrange multipliers associated with the constrained bonds il and calculated through[9]

$$-(\mathbf{F}_n \cdot \mathbf{R}_n + \dot{\mathbf{R}}_n^{\,2}) = \sum_{n'} (\mathbf{R}_n L_{nn'} \cdot \mathbf{R}_{n'}) \lambda_{n'} \tag{14}$$

which is a linear matrix equation. In eq 14, $\mathbf{R}_n$ is a bond vector (difference in position vectors between the atoms i and l, connected through bond n, whose length is constrained at R_0), $\mathbf{F}_n$ is the difference in systematic forces (i.e., forces due to V_{tot}) on the two ends of bond n, and $\mathbf{L}$ is a band matrix that "selects" the other constraints in which the sites of bond n are involved (details in ref 9). Once the systematic forces have been calculated, eq 14 can be solved for the set of λ_n, and then, through eq 11, the accelerations can be extracted. P_{int} is the instantaneous pressure of the system, calculated from interatomic forces by the atomic virial expression[11]

$$P_{\text{int}} = \frac{1}{3L^3} \sum_i \left(m_i \dot{\mathbf{r}}_i^{\,2} - \sum_j \sum_{\zeta} r_{ij}^{\zeta} \frac{\partial V_{\text{tot}}}{\partial r_{ij}^{\zeta}} + \sum_l \lambda_n r_{il}^{\,2} \right) + P_{\text{tail}} \tag{15}$$

The tail contribution P_{tail} is computed from the instantaneous density by direct integration, as explained in eq 1.4 of ref 11. In our early runs, both atomic and molecular virial pressure[11] were calculated and their running average values were found to coincide with each other and with the set value of pressure. Moreover, we noticed that there was no significant change in the stability of integration if the instantaneous molecular virial pressure were used in place of the atomic virial pressure in eq 15. This led us to use the instantaneous molecular virial pressure as P_{int} in our production runs,

Table 2. Thermodynamic Properties

property	conditions	simulation prediction	experimental value
$\alpha_P = \Delta\langle V\rangle/(\langle V\rangle\Delta T)$	$T = 300, 353$ K $P = 10$ MPa	$(3.4 \pm 0.5) \times 10^{-4}$ K^{-1}	3.4×10^{-4} K^{-1}
$\kappa_T = [\langle V^2\rangle - \langle V\rangle^2]/(\langle V\rangle k_B T)$	$T = 300$ K $P = 10$ MPa	$(5.0 \pm 0.7) \times 10^{-4}$ MPa^{-1}	4.9×10^{-4} MPa^{-1}
$\delta = \sqrt{\langle E_{coh}/V\rangle}$	$T = 300$ K $P = 10$ MPa	13.9 ± 0.3 (J/cm^3)$^{1/2}$	15.4 (J/cm^3)$^{1/2}$

since it has contributions only from nonbonded intermolecular interactions, and is therefore much more economical computationally. The conserved quantity in this extended system is the augmented Hamiltonian

$$H = \sum_i \frac{\mathbf{p}_i^2}{2m_i s^2} + V_{\text{tot}} + \frac{p_s^2}{2Q} + fk_B T \ln s + \frac{p_L^2}{18WL^4} + P_{\text{ex}}L^3 + \frac{1}{2}\sum_n \lambda_n (R_n^2 - R_0^2) \quad (16)$$

where

$$\mathbf{p}_i = \frac{\partial L}{\partial \dot{\mathbf{r}}_i} = m_i s^2 \dot{\mathbf{r}}_i^2 \qquad p_s = \frac{\partial L}{\partial \dot{s}} = Q\dot{s}$$

$$p_L = \frac{\partial L}{\partial \dot{L}} = 9WL^4\dot{L}$$

Simulations were performed at pressures P ranging from 1 to 1000 atm and temperatures T ranging from 273 to 600 K. A variable, self-adjusting time step method was implemented, which ensured that the absolute deviation between predicted and corrected accelerations was less than 5×10^{-4} times the magnitude of the acceleration. The exclusion of high-frequency vibrating HCH bond angles resulted in an average time step of 0.8 fs, which is significantly larger than in previous work (ca. 0.4 fs).[3] The initial configurations were produced through molecular mechanics[1] and equilibrated for 100−1000 ps, depending on the temperature simulated. Stabilization of the running average for the density and the various components of the energy was used as a criterion for starting data collection, i.e., starting the "production phase" of the run. Most properties were obtained from analysis of 1-ns-long trajectories.

3. Results and Discussion

***PVT* Behavior and Thermodynamic Properties.** With the potential parametrization adopted here, satisfactory predictions are achieved for the volumetric properties over a wide range of temperature and pressure. The predicted specific volume at $P = 1$ atm is shown as a function of temperature in Figure 2. Error bars result from averaging the results of *NPT* MD runs started at different initial configurations. Simulated values are within 3% of experiment. In Table 2 a comparison is shown between simulated and experimental values of the isobaric thermal expansivity, isothermal compressibility, and Hildebrand's solubility parameter. The methods of calculation and the conditions simulated are indicated on the table. The expansivity was obtained from numerical differentiation of the $V(T)$ prediction, wheras the compressibility was estimated from volume fluctuations in the *NPT* ensemble. The solubility parameter was calculated as the square root of the cohesive energy density, $\langle E_{coh}/V\rangle$. E_{coh} was estimated as the difference between the intramolecular energy of all "parent" chains and the total potential energy of the box, taking potential "tail" contributions into account.[1] The simulation prediction is compared with the value of diethyl ether, a good solvent for aPP.

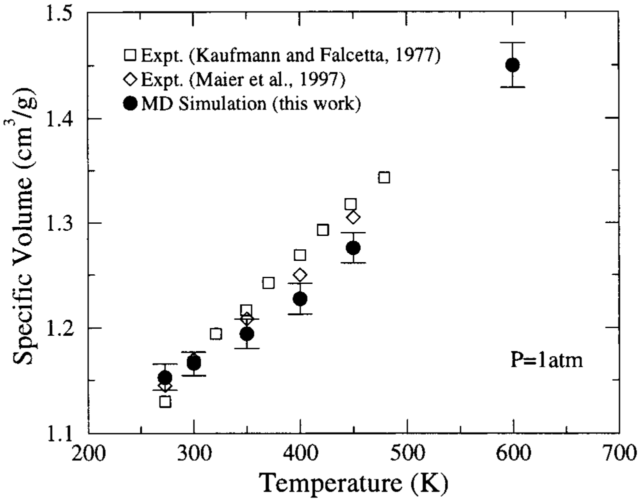

Figure 2. Dependence of the specific volume of atactic polypropylene at $P = 1$ atm on temperature as predicted by simulation and as measured experimentally.[16,17]

Structural Features. The structure of the polymer was examined by calculating the simulated X-ray diffraction pattern. The static structure factor at a given wave vector $\mathbf{k}$ can be defined as

$$S(k) = 1 + \frac{\left\langle \frac{1}{V} \right\rangle \sum_a \sum_b N_a N_b f^a(k) f^b(k) \int [g^{ab}(r) - 1] e^{-i\mathbf{k}\cdot\mathbf{r}}\, d^3r}{\sum_a [f^a(k)]^2} \quad (17)$$

The radial distribution functions $g^{ab}(r)$ for each pair of groups (a, b) in the system (a, b = CH, CH_2, CH_3) and the inverse system volume $1/V$ were accumulated and averaged for each structure, at a given temperature. The terms N_a and $f^a(k)$ are the number and atomic scattering factor, respectively, of atomic groups of type a. The atomic scattering factors of CH, CH_2, and R = CH_3 were calculated through an analytical approximation described in ref 19. In Figure 3 a simulated diffraction pattern is presented along with experimental data.[18] The positions and the magnitudes of the major intermolecular peak near $k = 1.1$ Å^{-1} and intramolecular peaks near 3.0 and 5.0 Å^{-1} agree well with experiment, indicating that the structure of the simulated polymer is realistic.

Torsional angle distributions at 300 and 600 K are presented in Figure 4. The five rotational isomeric states (RIS) for aPP torsion angles according to Suter and Flory[20] are also indicated on this figure. At these

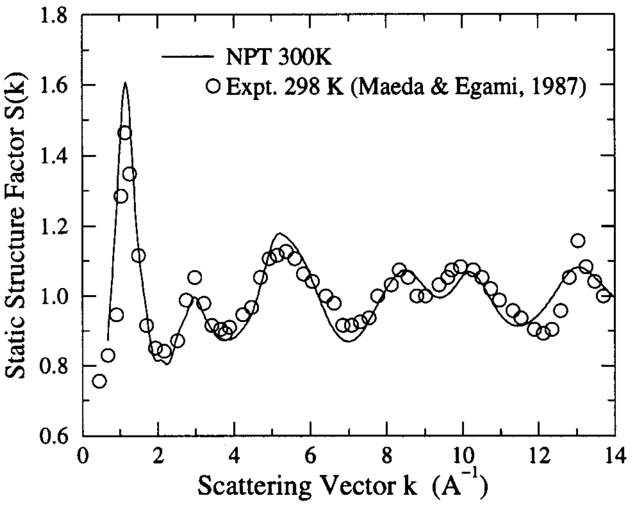

Figure 3. Simulated and experimental X-ray diffraction pattern of aPP near 300 K. The experimental measurements were made by Maeda[18] using angular scanning X-ray diffraction with a synchrotron radiation source.

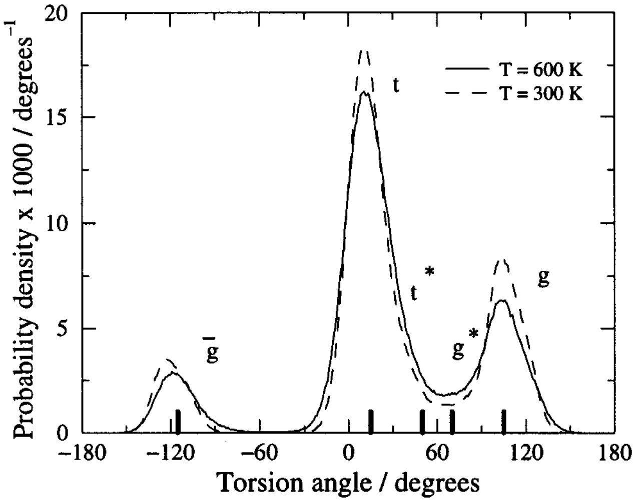

Figure 4. Simulated torsion angle distributions of aPP melt. Results are shown for atmospheric pressure *NPT* simulations at 600 K (solid) and 300 K (dashed). The convention for measuring torsion angles is as in ref 1. *trans*(t,t^*) and *gauche*($\bar{g}$,g^*,g) rotational isomeric states are denoted.

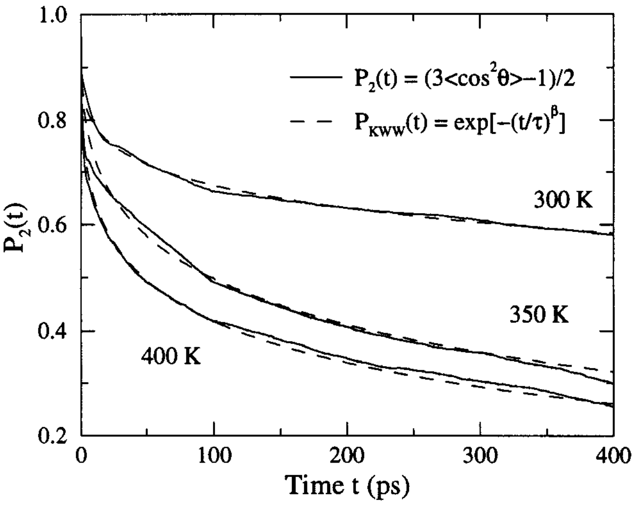

Figure 5. CR bond vector deccorrelation at various temperatures: (solid lines) simulation results; (dashed lines) KWW fits.

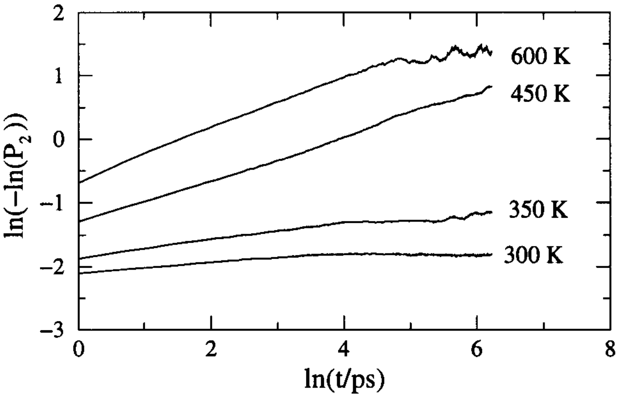

Figure 6. Typical double log−log plot of simulated CR bond vector decorrelation at various temperatures. The KWW stretching exponents β are found as slopes of the straight lines in such plots.

temperatures only $\bar{g}$, t, and g states are clearly evident. The t^* state is completely merged with t, resulting merely in a skewness in the t peak. The g^* state appears as a raised baseline between t and g peaks. The $\bar{g}$ state is significantly more populated than is predicted by the RIS model, an effect also seen in the molecular mechanics simulations of ref 1. As the temperature rises, one observes a broadening and lowering of the peaks, as expected.

Segmental Dynamics. Local dynamics was investigated by monitoring the rate of reorientation of C−R vectors. The directional autocorrelation functions for C−R vectors are defined as

$$P_1(i,t) = \langle \mathbf{u}_{CR}(i,t)\cdot\mathbf{u}_{CR}(i,0)\rangle \qquad (18)$$

$$P_2(i,t) = \frac{1}{2}(3\langle[\mathbf{u}_{CR}(i,t)\cdot\mathbf{u}_{CR}(i,0)]^2\rangle - 1) \qquad (19)$$

where $\mathbf{u}_{CR}(i,t)$ is the unit vector along the C_i−R_i bond at time t. The P_2 autocorrelation function, averaged over all i, is plotted in Figure 5 for several temperatures. As expected, the higher the temperature the shorter the time needed for a C−R bond to lose memory of its original orientation. The autocorrelation functions were fit with the Kohlrausch−Williams−Watts (KWW) equation

$$P_{KWW}(t) = \exp[-(t/\tau)^\beta] \qquad (20)$$

where τ is a characteristic decorrelation time and β is the stretching parameter. In order to facilitate comparison with the KWW expression, the $P_2(t)$ function is plotted for several temperatures in double logarithmic−logarithmic coordinates in Figure 6. The linearity observed suggests that the same stretched exponential behavior is followed out to 50 ps, beyond which poor sampling statistics precludes reaching a definitive conclusion at low temperatures. With the assumption that eq 20 holds out to very long times, we estimate correlation times for C−R bond orientational relaxation as

$$\tau_c = \int_0^\infty P_2(t)\,dt \Rightarrow \tau_c = \tau\frac{\Gamma\left(\frac{1}{\beta}\right)}{\beta}$$

with τ and β values extracted from the linear portion of

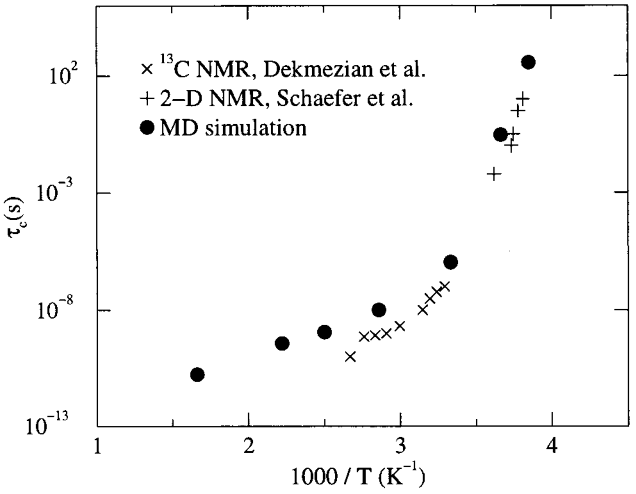

Figure 7. Temperature dependence of characteristic relaxation times for aPP bond vector decorrelations, averaged over many runs initiated at different configurations. Simulated values are calculated from KWW fits to the $P_2(t)$ function via $\tau_c = \tau\Gamma(1/\beta)/\beta$.

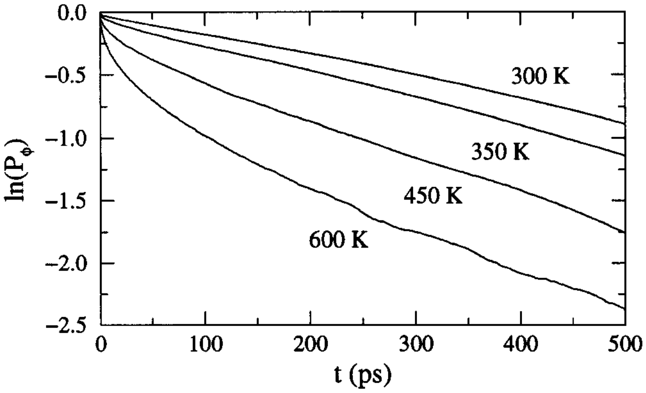

Figure 8. Semilogarithmic plot of simulated torsional autocorrelation function $P_\phi(t)$ at various temperatures.

the curves in Figure 6. KWW approximations to the $P_2(t)$ data based on these values are plotted in Figure 5 as broken lines. The resulting τ_c can be directly compared with NMR experiments of Dekmezian *et al.*[22] and Schaefer *et al.*[21] and are shown in Figure 7. Four different initial structures have been used to produce these relaxation times. For predictions at high temperatures, 1-ns-long equilibration runs were sufficient, but for lower temperatures (T < 350 K) runs of up to 5 ns were needed, depending also on the structure used. The temperature dependence of τ_c is distinctly non-Arrhenius. In a manner similar to experimental measurements, simulation predictions display a Williams–Landel–Ferry (WLF) behavior as the melt is cooled, approaching the glass temperature (experimental $T_g \simeq$ 255 K for aPP).

Local dynamics can also be probed by monitoring the torsional angle autocorrelation function

$$P_\phi(t) = \frac{\langle \cos \phi(t) \cos \phi(0)\rangle - \langle \cos \phi(0)\rangle^2}{\langle \cos \phi(0) \cos \phi(0)\rangle - \langle \cos \phi(0)\rangle^2} \qquad (21)$$

where $\phi(t)$ is the torsion angle at time t. P_ϕ values for several temperatures are displayed in Figure 8 in semilogarithmic coordinates and in Figure 9 in double logarithmic–logarithmic coordinates. Examination of these two figures indicates that the torsional autocorrelation exhibits close to an exponential decay at low temperatures and long times, suggesting that the dominant motions involved in the decorrelation are random librations of torsion angles confined within local energy wells. At high temperature (T = 600 K), on the other hand, the decay is almost perfectly KWW, indicating an abundance of conformational transitions involving motions of whole segments, the multiplicity in local environments encountered by these segments giving rise to stretched exponential behavior. Similarly intriguing behavior in $P_\phi(t)$ has been reported for n-$C_{44}H_{90}$ melts by Smith *et al.*[23] It should be emphasized, however, that the decay of $P_\phi(t)$ does not become purely exponential even at the lowest temperature studied; if it did, the 300 K curve in Figure 8 would appear as a straight line of slope 1. Rather, a systematic growth of the short-time KWW-like part at the expense of the long-time exponential-like part of $P_\phi(t)$ is seen as temperature is increased. The issue of nonexponentiality of torsion angle autocorrelation functions at short times has been discussed by Kim and Mattice.[24]

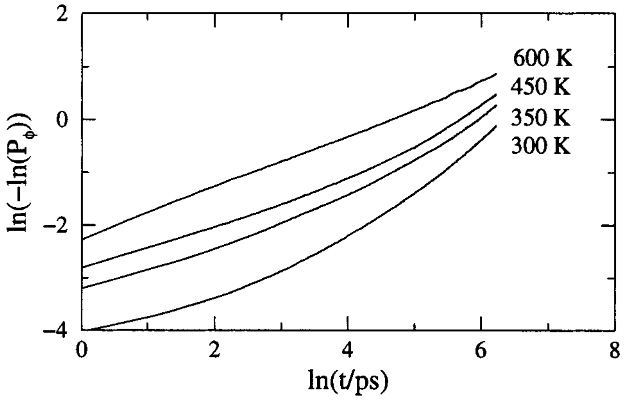

Figure 9. Typical double log–log plot of simulated torsional autocorrelation function $P_\phi(t)$ at various temperatures.

Table 3. Number and Rate of Conformational Transitions

temp (K)	successful crossings, N^{BC}	rate, k^{BC} (ps^{-1})
300	240	0.8
450	1627	5.4
600	6084	20.3

The last feature of dynamical behavior we analyzed was conformational transition rates, using two different methods. The first method is based on the Weber and Helfand[28] approach, which considers a transition of a torsion angle i to be complete only when ϕ_i has surmounted the potential barrier separating two conformational states and reached the bottom of the potential well of the new state. An estimate of the overal rate, k^{BC}, of well-to-well passages was calculated by[3]

$$k^{BC} = N^{BC}/N_\phi t_{run} \qquad (22)$$

where N^{BC} is the number of successful crossings, N_ϕ = 300 torsion angles in the system, and t_{run} is 1 ns. For three different temperatures the results are presented in Table 3.

Conformational transition rates have been determined for each ϕ_i in the system and are shown together with the average k^{BC} for each temperature in Figure 10. We observe that, as temperature rises, the number of angles undergoing transitions increases and the individual rates also rise. It is also evident that, at low

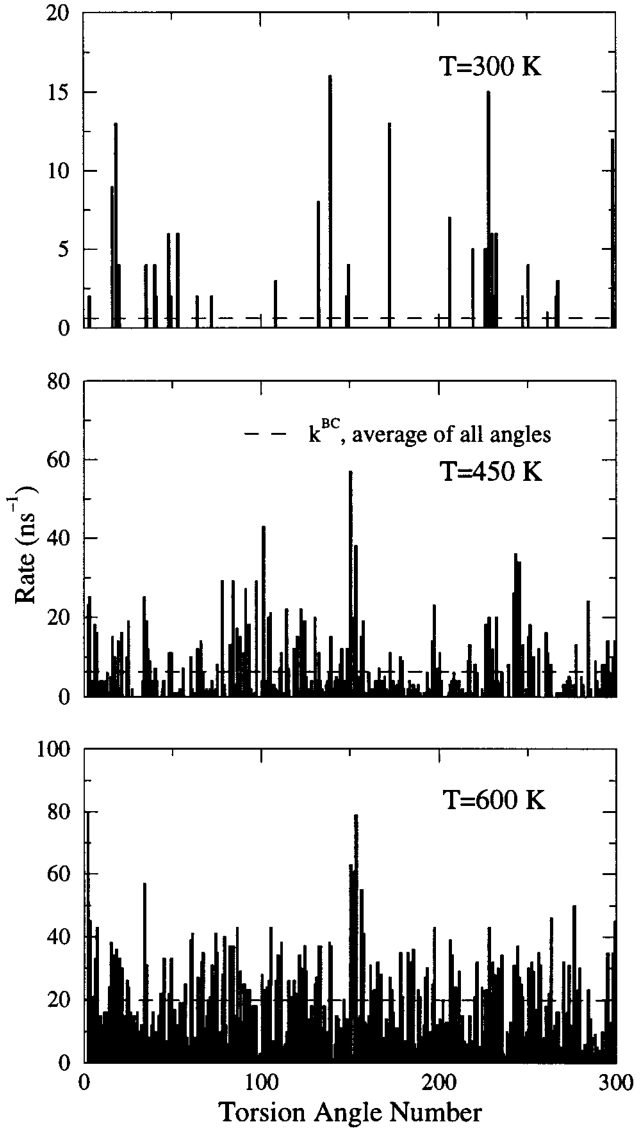

Figure 10. Individual conformational transition (well-to-well passage) rates for all torsion angles, calculated from 1-ns-long MD simulations at three temperatures. The numbering convention used is such that the angles 1−150 correspond to the first chain and 151−300 to the second chain. Dashed horizontal lines: average well-to-well passage rate at each temperature.

temperature, dihedral angles with nonzero transition rate are grouped together along chains, implying some same-chain cooperativity in this type of motion. Qualitatively similar findings have been reported from molecular dynamics simulations of an atactic polypropylene thin film[3] at 233 K and of polyethylene melts,[29] as well as from Brownian dynamics simulations.[28,30]

The coordinates of all bonds involved in the N^{BC} observed conformational transitions are plotted in Figure 11 at three different temperatures. Each sphere is placed at the center of a C−C bond that underwent at least one conformational transition within the time of observation (1 ns). At high temperature, all torsion angles appear susceptible to conformational transition, as expected. As temperature decreases, however, clusters of high local mobility appear, separated by large "frozen" regions. This clustering comes partially from the correlation of conformational isomerizations along a chain (see Figure 10) as well as from strong intermolecular correlations between neighboring chains. It should be noted that dynamic heterogeneity in connection with the low-temperature behavior of supercooled liquids has recently received considerable attention and has been an object of several simulation studies of simple model glass-forming fluids.[25−27]

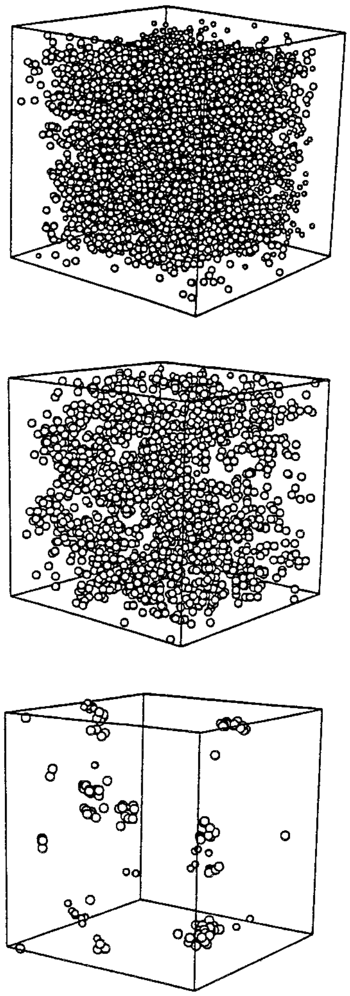

Figure 11. Spatial distribution of conformational transitions observed during 1-ns-long MD runs carried out on the same structure. Each sphere marks the center of a C−C bond that has experienced at least one conformational transition. Key: (top) 600 K; (middle) 450 K; (bottom) 300 K.

A different way to calculate the rate of conformational transitions is the construction of hazard plots.[30] The hazard rate $h(t)$ is defined such that $h(t)\,\mathrm{d}t$ is the probability that a bond, which has not had a transition in a time t since its last transition, undergoes a transition (first passage) between t and $t + \mathrm{d}t$. The cumulative hazard function is defined as

$$H(t) = \int_0^t h(t')\,\mathrm{d}t' \qquad (23)$$

The hazard plot was constructed as described in ref 3. For an ordered set of n time entries ($l = 1, 2, ..., n$) representing observed time intervals between successive conformational transitions of bonds, the cumulative hazard corresponding to the mth time entry is calculated from

$$\mathrm{H}_m = \sum_{l=1}^{m} \frac{1}{n + 1 - l} \qquad (24)$$

where $m \leq n$. For a Poisson process, the hazard plot would be a straight line with slope equal to the rate of

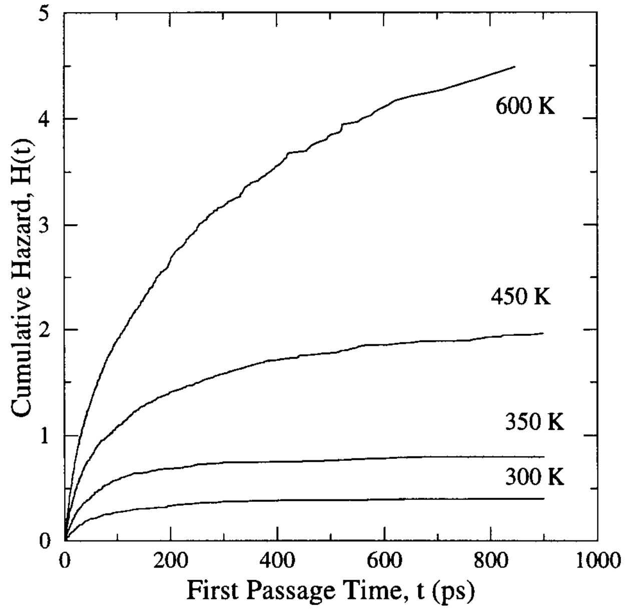

Figure 12. Hazard plot of first passage times for conformational transitions at several temperatures.

conformational isomerization. Such behavior has been seen in MD simulations of polyethylene melts.[23] As shown in Figure 12, such simple rectilinear behavior is not seen in atactic polypropylene out to times of 1 ns, even at the highest temperature studied. The strongly curved part of H(*t*) at short times provides evidence for recrossing events: an angle undergoing torsional isomerization is likely to cross back after a time that is short relative to the mean interval between barrier crossings averaged over all angles. The flattening out of H(*t*) at low temperatures and long times indicates that only a small fraction of the torsion angles are responsible for most of the observed transitions. These are the angles confined within the mobile regions of Figure 11 (bottom); they switch relatively fast between torsional states, while being surrounded by a matrix that does not undergo any significant torsional isomerization within the observation time of 1 ns. This behavior has first been reported in the simulations of Mansfield and Theodorou.[3]

4. Conclusions

In this work, a new molecular model has been developed for the prediction of thermodynamic and dynamical properties of polypropylene. An improved representation of the potential has been used, which differentiates between local and nonlocal interactions. Molecular dynamics simulations of atactic polypropylene using the new potential have been performed. Information on the structure and dynamics has been accumulated from 1-ns-long production runs.

Volumetric, thermodynamic, and structural properties have been calculated from *NPT* runs at a wide range of temperatures and pressures. The simulated specific volume vs temperature curve at $P = 1$ atm is within 3% of experiment. The thermal expansivity, calculated from the slope of the isobar at 1 atm, the isothermal compressibility, calculated from fluctuations of the volume at constant *P*, and the solubility parameter are also in good agreement with experimental values. The simulated X-ray diffraction pattern agrees well with experimental scattering results, suggesting that the simulated structure is realistic.

Several features of segmental dynamics of the system have been examined. Directional autocorrelation functions have been calculated for pendant (C−R) bonds above the glass temperature. Predicted correlation times, using KWW fits, are in good agreement with NMR measurements, the temperature dependence of these times exhibiting a WLF behavior. Simulated torsion angle autocorrelation functions display a KWW decay at high temperature and an exponential decay at low temperature. This observation suggests that, when the temperature is low, the directional decorrelation of pendant bonds is dominated by librations of torsion angles, while, as temperature rises, torsional transitions become more widespread and extended segmental motions appear, resulting in a spectrum of relaxation times. The development of a spatial heterogeneity in the segmental mobility as temperature decreases was detected directly through analysis of conformational transitions in dynamical trajectories of a given duration (1 ns); at low temperature, bonds capable of isomerizing conformationally are confined within small disjoint regions of the polymer. The rate of conformational transitions in the polymer has been analyzed by constructing a hazard plot of first passage times, which indicates strong deviations from Poisson process statistics and a sharp decrease in the number of bonds capable of conformational isomerization at low temperature.

Acknowledgment. We are indebted to Dr. Michael Greenfield for his valuable help in the development of the MD code and for sharing with us his derivation of the Fixman potential and of the chirality-preserving potential for polypropylene. The General Secretariat of Research and Technology of Greece is gratefully acknowledged for partial support of this work through a PENED'95 grant, No. 218.

A. Appendix

To sample the flexible model in the limit of infinite stiffness with MD using holonomic constraints, it is necessary to add fictitious forces, called "Fixman forces" (derived from a "Fixman potential"[10]), which compensate for the difference in the form of the kinetic energy function between the rigid and flexible models.[31] The Fixman potential for each chain is

$$V^{\mathrm{F}} = \frac{1}{2}k_{\mathrm{B}}T \ln \det \mathbf{h}_{N_{\mathrm{un}}} \tag{A.1}$$

Each element of the matrix $\mathbf{h}_n$ has the form

$$(\mathbf{h}_n)_{ij} = \sum_k \frac{1}{m_k} \sum_\zeta \frac{\partial q_i}{\partial r_k^\zeta} \frac{\partial q_j}{\partial r_k^\zeta}$$

where q_i and q_j are the hard (constrained) degrees of freedom (here bond lengths) and r_k^ζ are the position coordinates of heavy atoms, with index k ranging over all heavy atoms on the chain. The only terms of $\mathbf{h}_{N_{\mathrm{un}}}$ that are nonzero are those for which the expressions for the bond lengths q_i and q_j contain common Cartesian coordinates; see Table 4. Each skeletal bond length is of the form

$$q_i = l_i = [(x_i - x_{i-1})^2 + (y_i - y_{i-1})^2 + (z_i - z_{i-1})^2]^{1/2}$$

Table 4. Individual Terms in Matrix $\mathbf{h}_n$

q_i	q_j	$(\mathbf{h}_n)_{ij}$	abbrev
l_i	l_i	$1/m_i + 1/m_{i-1}$	s_i
l_i	l_{Ri}	$-(1/m_i)\cos\alpha_i$	v_i
l_i	l_{i+1}	$-(1/m_i)\cos\theta_i$	t_i
l_{Ri}	l_{Ri}	$1/m_{Ri} + 1/m_i$	u_i
l_{Ri}	l_{i+1}	$-(1/m_i)\cos\beta_i$	w_i
l_{i+1}	l_{i+1}	$1/m_{i+1} + 1/m_i$	s_{i+1}
l_{i+1}	l_{i+2}	$-(1/m_{i+1})\cos\theta_{i+1}$	t_{i+1}

Each derivative with respect to a Cartesian coordinate takes the form

$$\frac{\partial l_i}{\partial x_i} = \frac{x_i - x_{i-1}}{l_i} \qquad \frac{\partial l_i}{\partial x_{i-1}} = -\frac{x_i - x_{i-1}}{l_i}$$

and similarly for y- and z-derivatives. The derivatives involving pendant C−R bonds are obtained analogously. After taking the product of the two derivatives and summing over all heavy atoms, the resulting terms take the forms listed in Table 4. In terms of the abbreviations listed in Table 4, the following recursion relation holds:[6]

$$h_n = (\mathrm{H}_n - L_n u_{2n-3})h_{n-1} - (L_n \Lambda_n)h_{n-2} \qquad \text{(A.2)}$$

where $h_n = \det \mathbf{h}_n$ and

$$\mathrm{H}_n = \det\begin{pmatrix} s_{2n-1} & v_{2n-1} & t_{2n-1} \\ v_{2n-1} & u_{2n-1} & w_{2n-1} \\ t_{2n-1} & w_{2n-1} & s_{2n} \end{pmatrix}$$

$$L_n = \frac{s_{2n}u_{2n-1} - {w_{2n-1}}^2}{s_{2n-2}u_{2n-3} - {w_{2n-3}}^2}\,{t_{2n-2}}^2$$

$$\Lambda_n = (t_{2n-3}u_{2n-3} - v_{2n-3}w_{2n-3})^2$$

For each chain, the value of $h_{N_{\mathrm{un}}}$ is calculated by invoking the above relations from chain start ($n = 2$) to chain end ($n = N_{\mathrm{un}}$), using as initial values $h_0 = h_1 = 1$. The Fixman potential itself was calculated from eq A.1 above, after evaluating h_n from the recursion relation, eq A.2. Fixman forces were obtained through similar recursive relations derived by partial differentiation of eq A.2 with respect to heavy atom coordinates.

References and Notes

(1) Theodorou, D. N.; Suter, U. W. *Macromolecules* **1985**, *18*, 1467.

(2) Sylvester, M. F.; Yip, S.; Argon, A. S. In *Computer Simulation of Polymers*; Roe, R.-J., Ed.; Prentice Hall: Englewood Cliffs, NJ, 1991; p 105.

(3) Mansfield, K. F.; Theodorou, D. N. *Macromolecules* **1991**, *24*, 6283.

(4) Han, J.; Boyd, R. H. *Macromolecules* **1994**, *27*, 5365.

(5) Boone, T. D. Prediction of Glass-Melt Behavior and Penetrant Sorption Thermodynamics in Vinyl Polymers via Molecular Simulations. Ph.D. Thesis, University of California at Berkeley, 1995.

(6) Greenfield, M. L. Molecular Modeling of Dilute Penetrant Gas Diffusion in a Glassy Polymer using Multidimensional Transition-State Theory. Ph.D. Thesis, University of California at Berkeley, 1996.

(7) Nosé, S.; Klein, M. L. *Mol. Phys.* **1983**, *50* 1055.

(8) Gear, C. W. *Numerical Initial Value Problems in Ordinary Differential Equations*; Prentice Hall: Englewood Cliffs, NJ, 1971.

(9) Edberg, R.; Evans, D. J.; Morriss, G.P. *J. Chem. Phys.* **1986**, *84*, 6933.

(10) Fixman, M. *Proc. Nat. Acad. Sci. U.S.A.* **1974**, *116*, 249.

(11) Theodorou, D. N.; Boone, T. D.; Dodd, L. R.; Mansfield, K. F. *Makromol. Chem., Theory Simul.* **1993**, *2*, 191.

(12) Dodd, L. R.; Boone, T. D.; Theodorou, D. N. *Mol. Phys.* **1993**, *78*, 961.

(13) Dodd, L. R.; Theodorou, D. N. *Adv. Polym. Sci.* **1994**, *116*, 249.

(14) Widmann, A. H.; Laso, M.; Suter, U. W. *J. Chem. Phys.* **1995**, *102* (14), 5761.

(15) Goldstein, H. *Classical Mechanics*, 2nd ed.; Narosa Publishing House: New Delhi, 1993.

(16) Kaufmann, H. S.; Falcetta, J. J. *Introduction to Polymer Science and Technology: An SPE Textbook*; Wiley, NY, 1977; p 244.

(17) Maier, R. D.; Thomann, R.; Kressler, J.; Mülhaupt, R. *J. Polym. Sci., Polym. Phys.* **1997**, *35*, 1135.

(18) Maeda, T. Structural Analysis of Atactic Polypropylene: A Study of The Glass Transition by X-ray Diffraction. Ph.D. Thesis, University of Pennsylvania, 1987.

(19) Narten, A. H. *J. Chem. Phys.* **1979**, *70*, 299.

(20) Suter, U. W.; Flory, P. J. *Macromolecules* **1975**, *8*, 765.

(21) Schaefer, D.; Spiess, H. W.; Suter, U. W.; Fleming, U. W. *Macromolecules* **1990**, *23*, 3431.

(22) Dekmezian, D. E.; Axelson, D. E.; Dechter, J. J.; Borah, B.; Mandelkern, L. *J. Polym. Sci.* **1985**, *23*, 367.

(23) Smith, G. D.; Yoon, D. Y.; Zhu, W.; Ediger, M. D. *Macromolecules* **1994**, *27*, 5563.

(24) Kim, E.-G.; Mattice, W. L. *J. Chem. Phys.* **1994**, *101*, 6242.

(25) Yamamoto, R.; Onuki, A. *Europhys. Lett.* **1997**, *40*, 61.

(26) Kob, W.; Donati, C.; Plimpton, S. J.; Poole, P. H.; Glotzer, S. C. *Phys. Rev. Lett.* **1997**, *79*, 2827.

(27) Perera, D. N.; Harrowell, P. *Phys. Rev. Lett.* **1998**, *81*, 120.

(28) Weber, T. A.; Helfand, E. *J. Chem. Phys.* **1983**, *87*, 2881.

(29) Takeuchi, H.; Roe, R-J. *J. Chem. Phys.* **1991**, *94*, 7446.

(30) Helfand, E.; Wasserman, Z. R.; Weber, T. A. *J. Chem. Phys.* **1979**, *70*, 2016.

(31) Gō, N; Scheraga, H. A. *Macromolecules* **1976**, *9*, 535.

MA9807318